Impact of the maturation process on soot particle aggregation kinetics and morphology

José Morán, Christophe Henry, Alexandre Poux, Jérôme Yon

▶ To cite this version:

José Morán, Christophe Henry, Alexandre Poux, Jérôme Yon. Impact of the maturation process on soot particle aggregation kinetics and morphology. Carbon, 2021, 182, pp.837-846. ⟨10.1016/j.carbon.2021.06.085⟩. ⟨hal-03281409⟩

HAL Id: hal-03281409

https://normandie-univ.hal.science/hal-03281409v1

Submitted on 2 Aug 2023

Impact of the maturation process on soot particle aggregation kinetics and morphology

José Morán[a], Christophe Henry[b,*], Alexandre Poux[a], Jérôme Yon[a,**]

[a]*Normandie Univ, UNIROUEN, INSA Rouen, CNRS, CORIA, 76000 Rouen, France.*
[b]*Université Côte d'Azur, Inria, CNRS, Cemef, France.*

Abstract

Mature soot aggregates exhibit a morphology which is currently mimicked by diffusion-limited aggregation (DLCA) codes, i.e. with a sticking probability = 1 when two aggregates collide. Nevertheless, nascent soot particles may grow in the reaction-limited aggregation regime (RLCA), i.e. with a sticking probability << 1. Yet, it remains to be seen how fast the transition from RLCA to DLCA occurs for soot particles and what is the impact on aggregation kinetics, particle size distribution and morphology. This work intends to fill this gap by exploring the aggregation of soot particles formed in a laminar premixed flame through numerical simulations. Results show that the transition from RLCA to DLCA is very fast and produces a moderate impact on soot formation dynamics and morphology. However, soot particles mass bulk density is found to play an important role and should be considered in future simulations of soot formation in flames.

Keywords: Soot, Maturity, Aggregation, Electrostatic, Van der Waal, Rebound

---

*Corresponding author. *Tel:* +33 492 387 703. *E-mail:* christophe.henry@inria.fr (Christophe Henry)
**Corresponding author. *Tel:* +33 232 953 600. *E-mail:* yon@coria.fr (Jérôme Yon)

Preprint submitted to Carbon *June 17, 2021*

---

1. Introduction

The incomplete combustion of hydrocarbon fuels leads to the formation of a variety of complex Polycyclic Aromatic Hydrocarbon (PAH) molecules. The clustering of these PAH molecules commonly leads to the formation of spheroidal nascent soot primary particles, which can reach sizes around a few nanometer [1–6]. This PAH clustering process is very complex. Molecular Dynamics simulations have provided important insights into the formation of these nascent soot primary particles. For instance, they have provided an estimation of soot available reactive sites and surface properties [7–9], molecular PAH cluster morphology [3, 10], internal structure [11, 12], detailed PAH molecules interactions and clustering [13]. These simulations have shown that smaller soot particles coalesce faster than larger ones [3, 12]. In this context, it is reasonable to consider a critical time t_2 (corresponding to a limit diameter d_c) after which$^{\mathrm{Rev}}$ agglomeration replaces coalescence leading to ramified structures also called fractal-like aggregates (see Fig. 1). This article focusses on what occurres after this stage, in particular on the role played by soot maturity (here the change in chemical composition and particles bulk density) on the aggregation kinetics and morphology.$^{\mathrm{Rev}}$ The formation of these complex aggregates can be modeled by classical Diffusion-limited Cluster Aggregation (DLCA) or Reaction-limited Cluster Aggregation (RLCA) codes when detailed information on aggregate's morphology is intended [14]. In this type of simulations, the motion of each individual particle is explicitly solved and agglomeration can occur when two particles collide. More precisely, DLCA and RLCA simulations assume that particles undergo purely diffusive motion (i.e. convective transport by an underlying flow is neglected). This means that these methods are restricted to small particles, typically within the colloidal range (i.e. lower than a few micrometers, for which gravity forces are negligible compared to Brownian motion). DLCA and RLCA simulations are able to produce morphologies similar to soot aggregates. The main difference between DLCA and RLCA simulations lies in the treatment of collisions between two particles: DLCA assumes that agglomeration is driven by particle diffusion while agglomeration is driven by the physico-chemical interactions between particles in RLCA codes. To put it differently,$^{\text{Rev}}$ in DLCA codes, every collision between a pair of particles leads to their adhesion and, hence, to the formation of aggregates (i.e. the sticking probability is 1). In RLCA codes, the sticking probability is close to 0, meaning that only a few collisions are successful to form an aggregate. In reality, nascent soot particles may have a very low sticking probability, i.e. they may rebound after collisions due to their higher mobility and lower potential well depths compared to mature soot [15]. On the contrary, mature soot have a higher tendency to form aggregates due to a sticking probability ≈ 1. Therefore, a second critical diameter d_s has to be considered as the transition between both regimes, as illustrated in Fig. 1. Little attention has been paid to this second critical diameter. Therefore, in the present work, we focus on identifying d_s. The question we intent to answer in the current investigation is the d_s sto simulate the transition from RLCA to DLCA and what would be the consequences on soot aggregation kinetics, morphology and size distribution?$^{\text{Rev}}$

This transition is expected to be related to the evolution of particle mobility and their composition. In fact, nascent particles are small (a few nanometers diameter) and have a mass bulk density ~ 1.2 g/cm^3 at typical flame temperatures [16] whereas, mature soot primary particles have a larger diameter, are solid, with a graphitic structure and a bulk mass density of ~ 1.8 g/cm^3 [16, 17]. Similarly, the chemical composition, parametrized by the C/H ratio, increases with maturity due to soot dehydrogenation [5, 18]. Indeed, soot maturity evolution has many physico-chemical consequences as further discussed in Refs. [19, 20]. These progressive modifications of the physico-chemical properties of soot particles may consequently induce a change of particle mobility but also affect their sticking probability [15, 21].

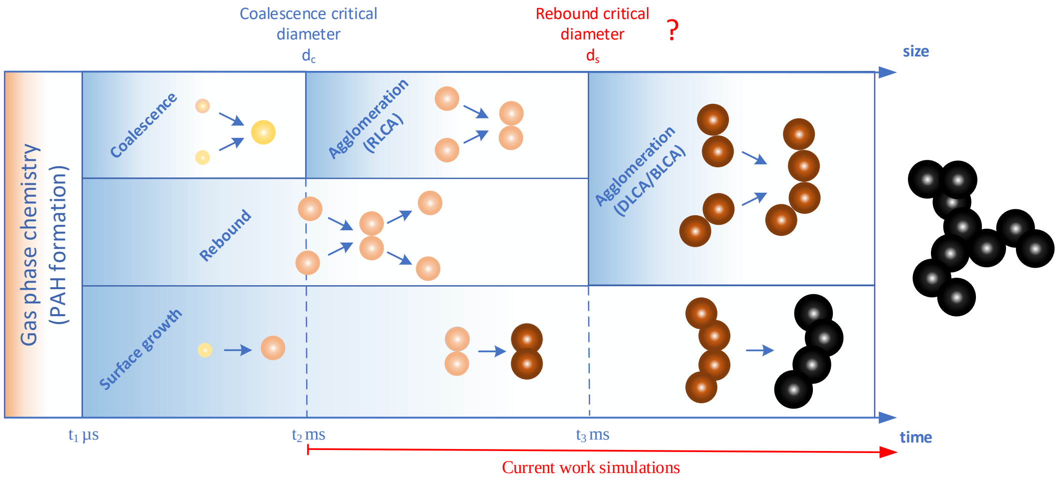

Figure 1: Different processes and mechanisms involved in soot formation in flames.

Another factor, commonly overlooked in the literature, is the role played by the particle electric charges. Different works have found soot particles to acquire a natural electric charge in flames due to chemi-ionization reactions and ion attachment to PAH clusters or primary particles [22–26]. The interaction between charged colloidal particles leads to the presence of repulsive electrostatic forces that can hamper agglomeration. Indeed, when the kinetic energy of the approaching particles is not strong enough to overcome the repulsive electrostatic forces, particles repel each other and prevent agglomeration [27]. Therefore, accurate predictions of the outcome of soot particle interactions require simulations that include both the sticking and the collision probabilities. To the authors' knowledge, such modifications of electrical properties have never been taken into account to study the morphological properties and kinetics of soot aggregation. The present work intends to fill this gap by considering the bulk density, sticking probability and electrostatic forces evolving in time. To this end, the Monte Carlo Aggregation Code (MCAC) [28] is used. This code allows the simultaneous transition in flow regime (from free-molecular to continuum) and agglomeration regime (from ballistic to diffusive) to be taken into account. It has been previously used to simulate soot agglomeration [29], and more recently agglomeration and surface growth [30]. As shown in Fig. 1, it is important to note that the dynamics of PAH molecular cluster formation is out of the scope of the present work. Here, we investigate the kinetics of non-coalescing soot primary particle aggregation and surface growth in a laminar premixed flame together with detailed calculations of inter-particle interactions.$^{\mathrm{Rev}}$

2. Methodology

To answer the main question raised by the current investigation, a physical evaluation of the collision and sticking probabilities of soot aggregates (described in Section 2.1) is carried out and then implemented in a Monte Carlo discrete element code as explained in section 2.3. The principle of the collision and sticking probabilities determination relies on fine-scale evaluations of the interaction energy between two soot aggregates (more details are provided in Section 2.2).

2.1. Interaction energy between particles

2.1.1. Interaction between primary spheres

Drawing on the previous study by Hou et al. [15], the interaction energy E between two spherical soot particles separated by a distance h is obtained by integrating the Lennard-Jones interactions between atoms over the volume of each body. This integration results in the sum of an attractive force and a repulsive force (more details can be found in [15] or a brief summary in Section 1 of the Supporting Material).

$$E_{\text{L-J}} = E_{\text{att}}(h) + E_{\text{rep}}(h) \tag{1}$$

The attractive term due to the van der Waals contribution can be written as

$$E_{\text{att}}(h) = -\frac{A_{ham}}{6} f_a\left(R_{p,1}, R_{p,2}, h\right) \tag{2}$$

where h is the separation distance between the two spheres, A_{ham} the Hamaker constant and f_a a function containing geometrical factors. The repulsive term is due to the overlap of electron orbitals occurring at very short separation distances. It is given by [15]:

$$E_{\text{rep}}(h) = \frac{1}{37800} A_{ham} \left(\frac{\sigma_{ab}}{2\,R_{p,1}}\right)^6 \left(U_{rep,1} + U_{rep,2} + U_{rep,3} + U_{rep,4}\right) \tag{3}$$

with σ_{ab} the distance of zero potential between atoms. Each of the four components $U_{rep,i}$ are detailed in Section 1 of the Supporting Material.

In addition to these short-ranged intermolecular forces, we also account for electrostatic interaction between charged soot particles. The formula for the potential energy of two charged spherical particles (each one having a given number of elementary charge z_p) is given by:

$$E_{\text{electro}}(h) = \frac{k_0\, z_{p,1}\, z_{p,2} e^2}{h} \tag{4}$$

where $k_0 = 8.9875517923 \times 10^9$ is the Coulomb constant (in $kg\, m^3\, s^{-2}\, C^{-2}$) and e is the elementary charge.

As a result, the total interaction energy E_{tot} between two primary soot particles is given by:

$$E_{\text{total}}(h) = E_{\text{att}}(h) + E_{\text{rep}}(h) + E_{\text{electro}}(h) \tag{5}$$

2.1.2. Parametrization

To solve Eq. (5), further information is required on particle properties. The Hamaker constant A_{ham} is estimated using the number density of carbon atoms (C) and hydrogen atoms (H) within each soot particle as well as the particle mass bulk density (similarly to the procedure in [15]). This means that, by changing the chemical composition of one particle and/or its density to account for maturity effects, the Hamaker constant is automatically updated to fit this new composition. Further details on the parametrization used here are provided in Section 1 of the Supporting Material. Soot particles charging may be determined by different mechanisms including the attachment of ions and electrons to soot molecular clusters, primary particles, and soot aggregates. Positive and negative ions are naturally produced in the flame as it has been experimentally observed [22, 31, 32]. These ions and electrons are believed to be produced mainly by chemi-ionization reactions [24]. However, thermo-emission may be an important mechanism to be considered. Indeed, Balthasar and Mauss [33] suggested that this mechanism might explain the appeareance of charged molecular clusters. More recently, Starik et al. [24] found no relevant role played by thermoemission. The relation between soot charging and maturity seems *a priori* not strong since flames with different fuels and different flame conditions show similar charge distributions [23, 25, 34, 35]. The detailed modeling of soot charging dynamics is beyond the scope of the present work (interested readers can refer to [24, 33, 36]). In this work, the electric charge of soot particles$^{\mathrm{Rev}}$ is estimated using available measurements on the charge distribution of soot particles in premixed flames [25]. Aggregates electric charges are obtained by randomly sampling a number of elementary charges (z_p) from the Boltzmann distribution [25],

$$f(z_p) = \left(\frac{K_E e^2}{\pi d_m k_B T}\right)^{1/2} \exp\left(\frac{-K_E z_p^2 e^2}{d_m k_B T}\right) \tag{6}$$

where $K_E = 9.0 \cdot 10^9$ Nm^2/C^2, k_B is the Boltzmann constant, e is the elementary charge, and d_m is the mobility diameter of the aggregate obtained from the friction coefficient of the aggregate [28, 30].

2.1.3. Interaction between aggregates

We further extend the previous work of Hou et al. [15] to compute the interaction energy between aggregates composed of a number of primary soot particles. As displayed in Figure 2, the difficulty that arises when computing the interaction between two aggregates is that it should take into account the aggregate morphology and its orientation with respect to the other aggregate/particle. In fact, depending on the aggregate morphology and orientation, one or several primary particles within a first aggregate can be in close proximity to other particles in the second aggregate. Hopefully, recent evaluations of van der Waals interactions between fractal DLCA aggregates have shown that the van der Waals interaction between aggregates is actually governed by the interaction between the closest pair(s) of primary particles [37]. This result is mainly due to the short-range nature of van der Waals forces, which usually act within the nanoscopic scale. As a result, we have simplified the present calculations of aggregate-aggregate interactions by accounting only for the interaction between the closest pair of primary particles.

Concerning electrostatic forces between aggregates, a similar issue arises since the exact repartition of charges within an aggregate is unknown. Several simplifications can be considered, including: (a) placing all charges on the closest pair of primary particles, (b) considering aggregates as full spheres with an equivalent radius where charges are homogeneously distributed and (c) placing all charges on the furthest pair of primary particles within aggregates. Since one of the objectives of this study is to assess the impact of electrostatic interaction on soot aggregation, we report here only the results obtained with case (a), which tends to overestimate the electrostatic contribution and thus corresponds to the worst case scenario.

2.2. Collision efficiency

As mentioned in the introduction, simulations of particle agglomeration require to couple a model for the aggregate transport (collision step) and a model for aggregate interactions (adhesion step). However, these two phenomena occur at various spatial and temporal scales: soot particles can indeed be transported near the flame over several centimeters while inter-aggregate forces are composed of short-ranged Lennard-Jones forces (within the nanoscopic scale) and long-range electrostatic forces. Since precise calculations of the combined motion of interacting aggregates at the nanoscopic scale are out of scope of the present study (it will require much smaller time steps for the transport model), the coupling of the two phenomena is obtained using energetic considerations that are similar to boundary conditions used in standard CFD simulations (see also [38]). This means here that only reduced information on the interaction energy is extracted from the whole energy-versus-distance curve (see also Fig. 2): the potential well $E_{well} \leq 0$ (i.e. the minimum of the interaction energy) and the energy barrier $E_{barr} \geq 0$ (i.e. the maximum of the interaction energy). As displayed in Fig. 2, three possible outcomes of an interaction are considered depending on the following energetic criteria:

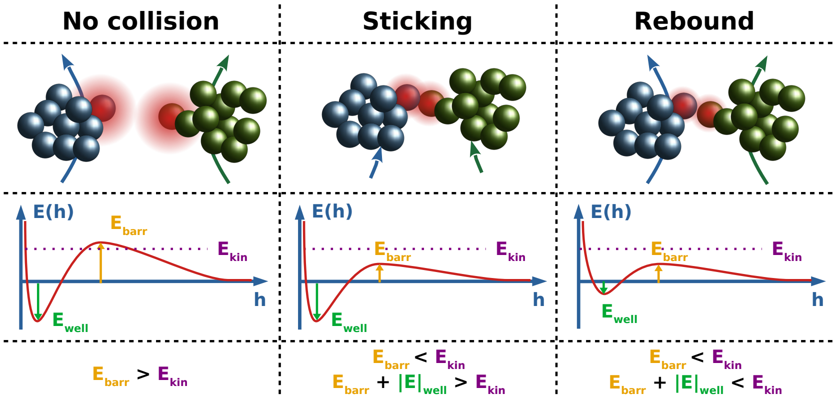

Figure 2: Sketch showing the three possible outcomes of a collision between two aggregates and the corresponding criteria (based on the potential well E_{well}, the energy barrier E_{barr} and the relative kinetic energy E_{kin}).

1. no collision occurs when the repulsive energy barrier E_{barr} overpowers the relative kinetic energy along the direction of collision E_{kin}, i.e. $E_{kin} < E_{barr}$;
2. a collision occurs when the relative kinetic energy along the direction of collision E_{kin} is high enough to overcome the repulsive energy barrier E_{barr}, i.e. $E_{kin} > E_{barr}$. Once a collision occurs, two subsequent results are possible:
   - 2.a. The two particles/aggregates stick to each other when the particle cannot escape the potential well, i.e. $E_{kin} < |E|_{well} + E_{barr}$;
   - 2.b. The two particles/aggregates rebound when their kinetic energy (again taken equal to the incoming one) prevails over the potential well, i.e. $E_{kin} > |E|_{well} + E_{barr}$;

Drawing on this scenario for the outcome of an interaction between soot particles/aggregates, a collision probability and a sticking probability are evaluated. The formula for these probabilities are obtained by analogy with a Brownian diffusion of particles in a force field (more details are provided in Section 2 of the Supporting Material):

$$\begin{aligned} P_{coll} &= 1 - \mathrm{erf}\left(\sqrt{\widetilde{E_{barr}}}\right) + \sqrt{\widetilde{E_{barr}}} \times \exp\left(-\widetilde{E_{barr}}\right) \qquad (7) \\ P_{stick} &= \mathrm{erf}\left(\sqrt{\widetilde{E_{stick}}}\right) - \sqrt{\widetilde{E_{stick}}} \times \exp\left(-\widetilde{E_{stick}}\right) \qquad (8) \end{aligned}$$

with the dimensionless potential energies $\widetilde{E_{barr}} = E_{barr}/(k_B T)$ and $\widetilde{E_{stick}} = (|E|_{well} + E_{barr})/(k_B T)$ (k_B being the Boltzmann constant and T the flame temperature).

2.3. Integration in an Aggregation Code

The Monte Carlo Aggregation Code (MCAC) is a recent code developped to simulate the aggregation of nanoparticles by considering the transition in both flow and aggregation regimes. The latter corresponds to the transition between ballistic-limited cluster aggregation (BLCA) and DLCA during time [28, 29]. More recently, surface growth process has been implemented, enabling a physically-driven generation of realistic soot aggregates consisting of overlapping primary particles [30]. In the context of the current work, MCAC has been adapted to non-unitary collision and sticking probabilities. In this context, a collision-check step is done each time two aggregates come to close contact. The outcome of this check depends on a uniformly distributed random number $\delta_1 \in [0, 1]$ such that, particles collide when $\delta_1 \leq P_{coll}$, or repel each other when $\delta_1 > P_{coll}$. If collision is found, a second random number is generatd $\delta_2 \in [0, 1]$ such that, particles stick together after collision when $\delta_2 \leq P_{stick}$, or rebound when $\delta_2 > P_{stick}$. This procedure is inspired by the classical RLCA codes found in the literature [39, 40]. As explained in previous sections, P_{coll} and P_{stick} depend on both the electrostatic barrier, and Lennard-Jones potential well depth, respectively. These properties depend on the flame temperature, aggregate's mobility diameter, primary particle size and soot maturity. To simulate a time-evolving soot maturity, the properties of individual aggregates are introduced as new parameters in MCAC (includig the C/H ratio, the density ρ_p, and electric charge). The C/H ratio is correlated to the average primary particle size (within an aggregate) and used to determine ρ_p (see section 3 of the Supporting Material). The potential well depth is determined based on the diameter of the colliding primary particles. The electrostatic barrier is determined based on the electric charge of the interacting aggregates. Indeed, the mobility diameters of the approaching aggregates is obtained based on the friction coefficient of aggregates [28, 41]. Thus, equation (6) is used to sample a given charge for each aggregate that respects the Boltzmann distribution. This new version of MCAC allows to investigate the kinetics of aggregation, the particle size distribution, and aggregates morphology.

Kinetics of aggregation is studied by quantifying the time evolution of the aggregate number concentration $N(t)$ in $\#/\mathrm{m}^3$ and the monodisperse equivalent coagulation kernel k_{ii} in m^3/s. The latter is determined from the local slopes of $1/N(t)$ as done in Ref. [29].

Particle size distribution is studied in terms of the volume-equivalent radius. The morphology of particles is studied in terms of the population-based fractal dimension, and fractal prefactor obtained by a log-log fit of the fractal-law expressed as,

$$\frac{V_{agg}}{\overline{V_p}} = k_f \left(\frac{R_g}{R_{pv}} \right)^{D_f} \tag{9}$$

where, V_{agg} is the aggregate volume corrected by overlapping monomers and obtained based on the SBL library [42], $\overline{V_p} = 1/N_p \sum_{i=1}^{N_p} (\pi/6) d_{p,i}^3 = (4\pi/3) R_{pv}^3$ is the average primary particle volume, and R_g is the aggregate's radius of gyration obtained by discretizing the aggregate [41] (see section 4 of the Supporting Material). In addition, the pair correlation function for representative aggregates is calculated and fitted to search the packing factor φ which is an indicator of the local compacity in the cluster. The details on its determination are given elsewhere [43, 44] and the fitting procedure is the same than in Ref. [30]. Further details can also be found in section 5 of the

Supporting Material.

3. Results

3.1. Case studied and parametrization

A premixed ethylene flame ($C/O = 0.82$) is selected as a test case. This flame has been already simulated by considering the simultaneous aggregation and surface growth [30] but change of maturity was not considered and thus, the collision and sicking probabilities were fixed to 1. In order to start the current simulation with smaller primary particle size than in the aforementioned work, surface growth rates (u in nm/ms) from Ref. [30] have been linearly extrapolated to shorter residence times. Current simulations start at $t = 3.5$ ms, with 1024 spherical primary particles [45] corresponding to a lognormal size distribution with a geometric diameter of $d_p = 2.4$ nm and geometric standard deviation of 1.2. The domain size is set to respect the initial volume fraction to $f_v = 0.002$ ppm. Constant temperature $T = 1700$ K and 1 atm of pressure are considered. The simulation ends at $t = 30$ ms.

In this study, based on a literature survey, nascent soot are considered to have C/H = 1.1 and a corresponding bulk density of $\rho_p = 1.2$ g/cm^3. In contrast, mature soot are characterized by C/H = 10 and $\rho_p = 1.8$ g/cm^3. Mass bulk density of nascent and mature soot particles are obtained from [17], being in good agreement with [16].

Different cases are considered in order to evaluate the role played by maturity and electrostatic forces (see Table 1). The first one called "mature (no potentials)" consists in keeping the properties of mature soot during all the simulation and considering systematic collision and sticking when two aggregates approach each other (i.e. whatever the size of the colliding primary spheres). This corresponds to the usual DLCA approach. The second one called “nascent (no potentials)” is identical to the previous one but now considering the physical properties of nascent soot. The comparison with the previous case is then used to study the role played by the bulk density.

Cases 3 and 4 called respectively “mature (only LJ)” and nascent “(only LJ)” will also conserve the physical properties of respectively mature and nascent soot, but for these cases the sticking probabilities are evaluated based on the colliding primary particle radii according to the their composition.

Case 5 “variable maturity (LJ+electrostatic)” considers a transition of soot maturity induced by a variation of C/H and consequently in ρ_p according to the primary sphere radius based on Refs. [5, 46] (see the section 3 of the Supporting Material for further details). This case also considers the electrostic forces as described in Section 2.1.

For each case studied, a total of 10 simulations are conducted and results presented later are averaged over these ten simulations as done in previous works [29, 30].

3.2. Collision and sticking probabilities of soot particles

3.2.1. Effect of maturity

We first assess the role of soot maturity (expressed though particle size, mass bulk density and composition) on the collision and sticking probabilities. To this end, we evaluate the behaviour for mature soot, nascent soot and soot with variable maturity but zero electric charges. In that case, since no repulsive forces act on a range longer than van der Waals forces, no energy

Table 1: Selected cases for numerical simulations.

Case	Description
Mature (no potentials)	$P_{coll} = 1$ and $P_{stick} = 1$, $\rho_p = 1.8$ g/cm^3
Nascent (no potentials)	$P_{coll} = 1$ and $P_{stick} = 1$, $\rho_p = 1.2$ g/cm^3
Mature (only LJ)	$P_{coll} = 1$, and P_{stick} is evaluated, $\rho_p = 1.8$ g/cm^3, C/H = 10.0
Nascent (only LJ)	$P_{coll} = 1$, and P_{stick} is evaluated, $\rho_p = 1.2$ g/cm^3 C/H = 1.1
Variable maturity (LJ + electrostatic)	P_{coll} and P_{stick} are evaluated, ρ_p and C/H evolve in time electrostatic forces considered

barrier occurs (not shown here). Hence, the collision probability is always equal to unity. However, the balance between van der Waals forces and Born repulsion leads to an existing potential well whose value depends on the particle size as well as on the particle properties.

Figure 3 displays the evolution of the potential well and sticking probability as a function of the reduced particle radius $R_{red} = R_{p,1}R_{p,2}/(R_{p,1} + R_{p,2})$, where $R_{p,i}$ expresses the radius of the i'th colliding primary particle. Several conclusions can be drawn from this figure:

- when the particle properties are fixed (“mature” or “nascent” cases), the depth of the potential well increases with increasing reduced particle diameter. This is consistent with previous studies of neutrally charged particles (e.g. [15]). As a result, the sticking probability quickly increases from 0.1 at $R_{red} = 0.5$ nm to values close to 1 around $R_{red} = 3$ nm. Based on the definition of the reduced particle radius, we can evaluate the critical primary diameter at which the sticking probability is roughly equal to 1, which happens to be around $d_s \sim 8$ nm for nascent particles (resp. $d_s \sim 12$ nm for mature soot). This means that, except for very small particles, a collision does induce agglomeration of the two particles involved. This result is comparable to the one obtained by Hou et al. [15], who obtained $d_s \sim 14$ nm for soot particles at $T = 1500$ K. The slight difference is due to the different formula used to evaluate the sticking probability (see section 2.3 of the Supporting Material) as well as to differences in the density and C/H ratio considered for nascent or mature soot.

- the depth of the potential well for mature particles (and consequently the sticking probability) is higher than the one for nascent particles. This is related to the fact that mature particles have a higher Hamaker constant due to their higher density and C/H ratio, leading to stronger short-ranged repulsive forces.

- the results obtained with the variable maturity case are bounded by the two limit cases of “nascent” and “mature” particles. When one of the particle diameter is fixed, the depth of the potential well (and consequently the sticking probability) increases with the reduced particle diameter. Moreover, it clearly appears that the results obtained for the variable maturity case are very close to the "nascent" case when the reduced size is below 0.7 nm while they become very close to the "mature" case when the reduced size is above 4 nm (in which case, the sticking probability reaches a plateau value $P_{stick} \simeq 1$).

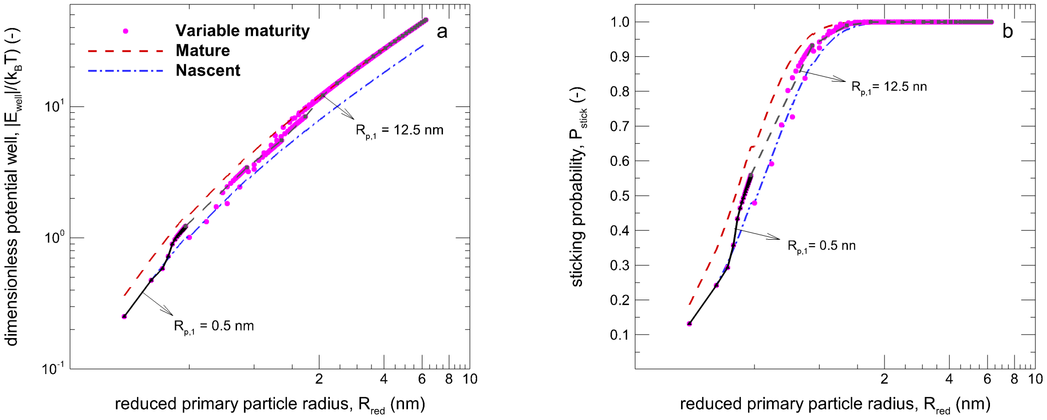

Figure 3: Evolution of the potential well (left) in absolute value, and sticking probability (right) as a function of the reduced particle radius $R_{red} = R_{p,1}R_{p,2}/(R_{p,1} + R_{p,2})$. Results obtained for spherical soot particles with zero electric charge and a size ranging between 1 and 25 nm. The particle density and C/H ratio are obtained either in the case of nascent soot, mature soot or variable maturity.

3.2.2. Effect of electrostatic forces

The role of electric charges on the interaction between soot particles has been assessed by changing the value of each particle charge between $-6e$ and $+6e$ while keeping all other properties fixed. Experimental determination of soot charge distribution in ethylene premixed flames [34] have reported to be narrow and symmetric within the $-2e$ to $+2e$ range for soot particles with mobility diameter $d_m \approx 13$ nm. As time evolves, this distribution considerably broadens but remains symmetric within the $-4e$ to $+4e$ for $d_m \approx 62$ nm. Indeed, Eq. (6) shows that the distribution of charges (z_p) is Gaussian distribution whose variance is $\sigma^2 = (d_m k_B T)/(2K_E e^2)$, thus increasing with mobility diameter of the aggregate (see section 7 in the Supporting Material). Based on these measurements, we have opted to consider a range of charges between -6e to +6e to ensure that all possible situations are covered.$^{\mathrm{Rev}}$

In the following, we consider the case of "variable maturity" particles with a fixed particle radius of 5 nm.

Figure. 4 displays 2D contours of the energy and probability values (E_{barr}, E_{well}, $\mathcal{P}_{coll}$, $\mathcal{P}_{stick}$) as a function of the elementary charge present in each particle. It can be seen that a range of values can be obtained depending on the elementary charge present in each particle. In particular, the collision and sticking probabilities are close to 1 only when particles have high but opposite charges. On the contrary, when both particles have a high and similar charges, the collision and sticking probabilities quickly drop to values close to 0.

Due to the symmetry in the effect of particle charges (see also Eq. (4)), we further analyse the effect of electrostatic charges by plotting the same results as a function of the product of the particle elementary charges $z_{12} = z_{p,1} z_{p,2}$. This is displayed in Figure 5. This allows to confirm and quantify the two aspects mentioned before. First, for similarly charged particles, the potential well is close to zero (except for $z_{12} << 1$) while the energy

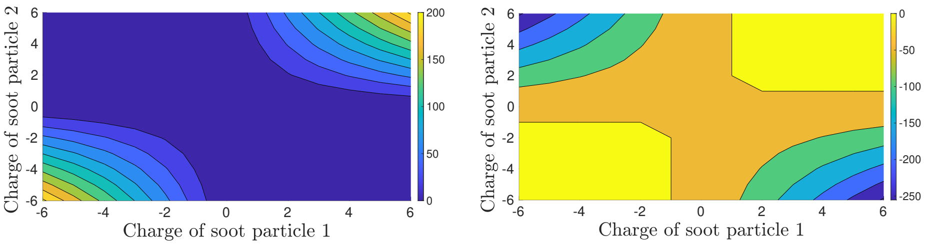

(a) Energy barrier (in k_BT)

(b) Potential well (in k_BT)

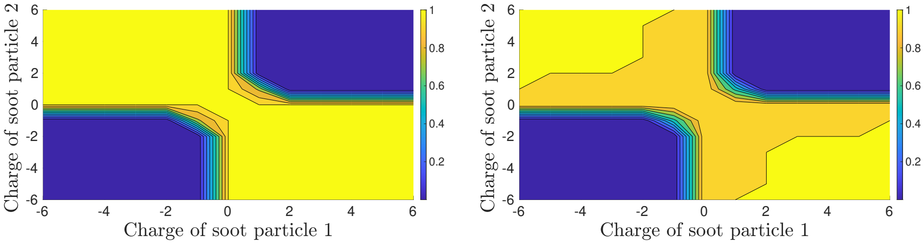

(c) Collision probability

(d) Sticking probability

Figure 4: 2D plot showing the evolution of $(\widetilde{E_{barr}}, \widetilde{E_{well}}, \mathcal{P}_{coll}, \mathcal{P}_{stick})$ as a function of the electric charge of each particle. Results obtained for spherical soot particles with $R_{p,1} = R_{p,2} = 5$ nm and variable maturity (density and C/H ratio).

barrier increases linearly with z_{12}. As a result, the collision probability (and hence the sticking probability) quickly drops to very small values when the particle charge increases. Second, for oppositely charged particles, no energy barrier occurs (except for $z_{12} << 1$) while the depth of the potential well is increased due to the attractive electrostatic force. In that case, both collision and sticking probabilities have values close to 1.

Although these results indicate a clear effect of soot maturity and electrostatic forces on the collision probability and sticking probability, it remains to be seen how this affects the actual agglomeration of soot particles. This is done in the next sections where these collision & sticking probaiblities are coupled to the MCAC code to simulate the formation and growth of soot

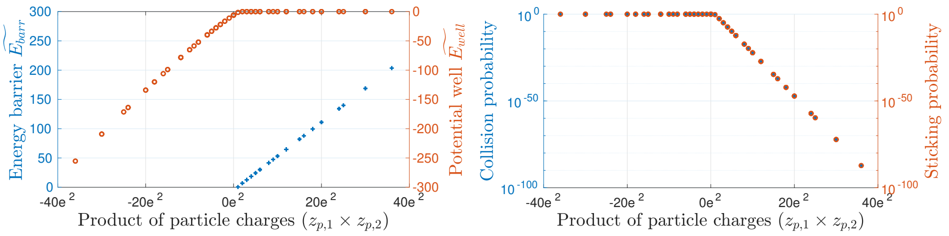

(a) Energy barrier & potential well

(b) Collision & sticking probability

Figure 5: Evolution of ($\widetilde{E_{well}}$, $\widetilde{E_{barr}}$, $\mathcal{P}_{coll}$, $\mathcal{P}_{stick}$) as a function of the product of the particle electric charges. Results obtained for spherical soot particles with a size of 5 nm. The particle density and C/H ratio are obtained with variable maturity.

aggregates.

3.3. Agglomeration of soot particles

Figure 6a presents the time evolution of the inverse particle number concentration $1/N(t)$. The local slope of this curve in log-log correspond to the kinetic exponent z, which indicates how fast aggregation is. The $1/N(t)$ is naturally increasing in time due to irreversible aggregation in the absence of continous nucleation and fragmentation. All cases show a similar evolution except in the cases of nascent soot particles. Indeed, nascent soot particles have a lower mass bulk density, consequenty they move faster and more ballistically. This leads to an enhanced kinetics of aggregation that becomes more evident over time. When comparing the two cases involving nascent soot (no potentials and only LJ), a clearer difference is observed at early residence times. Agglomeration is initially faster for the case without potential which is explained by the larger sticking probability (unity). However, the role played by bulk density seems relatively more important than taking into account of a time evolving sticking probability. This conclusion is reinforced by the comparison with the three remaining cases (mature with and without potentials and variable maturity). This means that considering the change of collision and sticking probability induced by the maturation process have a reduced impact on the aggregation kinetics. This is explained by the fact that d_s is very small, and also by the large surface growth efficiency (SGE) as shown in section 6 of the Supporting Material. This parameter has been introduced by [41] and quantifies the predominance of surface growth over aggregation to explain soot mass growth. For example, SGE $\rightarrow \infty$ means that surface growth dominates soot mass growth over aggregation, while SGE $\rightarrow 0$ means the opposite. In this work, non-unitary sticking or collision probabilities lead to larger values of SGEs, which is especially evident for early residence times. However at these residence times, the SGE is still high even without considering LJ or electrostatic potentials. The later is explained by the low nascent soot volume fractions making difficult to observe a big impact on the soot formation process.

However, when analyzing the kinetic exponents z obtained by a power-law fitting $1/N(t) \propto t^z$ for $t \in [23, 35]$ ms, other conclusions can be drawn. First, all the values correspond to aggregation in the transition regime since z is smaller than purely ballistic value ($z \approx 2.2$) and larger than purely diffusive ($z \approx 1$) regimes [29, 47]. Second, comparison between different simulations suggest that inclusion of the van der Waals sticking and electrostatic collision probabilities tends to accelerate agglomeration for large residence times (larger z). Third, comparing both cases involving purely LJ sticking probability reveals that nascent soot tends to agglomerate faster, with a kinetic exponent closer to the one for a purely ballistic regime. Nascent soot without potentials shows the lowest kinetic exponent explained by it faster aggregation at earlier residence times aproaching faster to transition regime where kinetic exponent could be as small as $z \approx 0.8$.

Fig. 6b reports the monodisperse equivalent coagulation kernel. This also expresses the agglomeration kinetics but is of great interest for soot modeling in CFD codes since kernels are essential to simulate aggregation by population balance methods. This representation is also complementary since it provides a larger sensitivity to the agglomeration processes at early residence times. Indeed, this highlights the rapid transition from low to high kernels at early residence times $t < 8$ ms (corresponding to $d_{p,geo} < 5$ nm) of the nascent soot composition depending on considering the collision and sticking probabilities or not. For larger residence times, the differences are mainly explained by the particles mass bulk density. Nascent soot particles coagulate faster due to their more ballistic motion, their larger collision surface and larger particle size polydispersity (see Fig. 6d).

The evolution of the geometric mean $R_{v,geo}$ (Fig. 6c) and geometric standard deviation $\sigma_{Rv,geo}$ (Fig. 6d) of the volume-equivalent radius of aggregates are also evaluated. The $R_{v,geo}$ parameter increases monotonically in time due to agggregation. Nascent soot leads to larger aggregate sizes due to the more efficienct aggregation process driven by lower bulk density as discussed above. In turn, the impact of maturation process, sticking probability or electrostatic repulsion is clearly negligible (no significant differences are observed when comparing all the cases related to mature soot). The $\sigma_{Rv,geo}$ reported in (Fig. 6d) expresses a more complex trend, in particular at early residence times. At these early residence times the decrease in polydispersity is linked to the dominance of surface growth in the competition with agglomeration (see section 6 of the Supporting Material), to produce larger soot aggregates [30]. Both cases considering nascent soot all along the simulation are characterized by more ballistic aggregation, consequently leading to larger $\sigma_{Rv,geo}$ for larger residence times, in agreement with previous observations [29, 30].

Table 2 summarizes the main morphological properties of aggregates sampled at the end of the simulation ($t = 30$ ms). The population-based fractal dimension (D_{fp}) and the corresponding fractal prefactor (k_{fp}) are reported, and further details on their determination are provided in section 4 of the Supporting Material. Overall, both D_{fp} and k_{fp} are very close for all the cases. Notably, the fractal dimension is larger than the one observed for DLCA aggregates $D_f = 1.78$, but smaller than BLCA $D_f = 1.91$ limits. Particularly, k_{fp} are considerably larger than those observed for aggregates formed by pure agglomeration in the absence of surface growth, whose values attain a maximum quite asymptotic limit ~ 1.4 [29]. The larger fractal prefactors observed in this work are explained by the increase in local compacity due to the overlapping of primary particles and the increase in the coordination number due to surface growth [30]. These values seem quite close to those determined experimentally [46, 48, 49]. The population averaged packing factors $\overline{\varphi}$ are also reported for the "Mature (LJ)" and "Nascent (LJ)" cases. As explained in the previous section, they are determined by fitting the pair correlation function for individual aggregates sampled at the end of the simulation ($t = 30$ ms). This parameter is related to the local compacity of primary particles, and has been found to increase with the

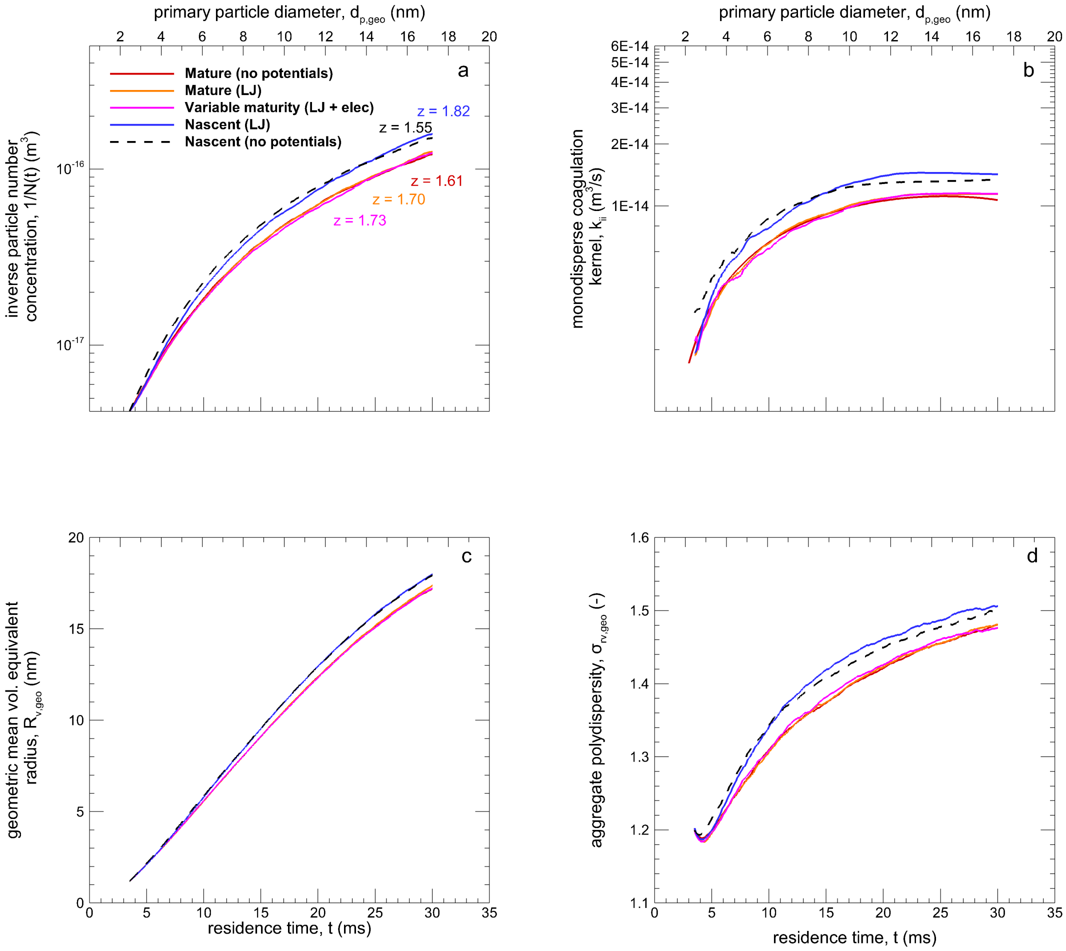

Figure 6: Time evolution of the inverse particle number concentration $1/N(t)$, monodisperse equivalent coagulation kernels, geometric mean volume-equivalent radius, and the corresponding geometric standard deviation.

number of monomers per aggregate. It attains a maximum value between 1 to 1.4 for DLCA aggregates consisting of 10^3 point-touching monodisperse and polydisperse monomers, respectively [44]. Current aggregates contain ~ 100 monomers per aggregate and their packing factor ($\overline{\varphi} \approx 1.5$) is larger than those found in the referred work. This is explained by primary particle overlapping [30]. These packing factors are in good agrement with [30] who obtained $\overline{\varphi} \approx 1.49$ for large aggregates ($N_p \in [430, 450]$) generated under the same flame conditions. However, no relevant difference is observed in local compacity for the different cases studied.

Table 2: Morphological parameters characterizing aggregates sampled at the end of the simulation ($t = 30$ ms). Population fractal dimension (D_{fp}), and prefactor (k_{fp}) as well as average individual packing factor ($\overline{\varphi}$) are reported. Error values lead to the 95% confidence intervals.

Case	Population		Individual
	D_{fp}	k_{fp}	$\overline{\varphi}$
Mature (no potentials)	1.85 ± 0.01	2.15 ± 0.01	-
Mature (LJ)	1.83 ± 0.01	2.18 ± 0.01	1.57 ± 0.08
Variable maturity (LJ+elec.)	1.82 ± 0.01	2.19 ± 0.01	-
Nascent (LJ)	1.86 ± 0.02	2.19 ± 0.02	1.49 ± 0.10
Nascent (no potentials)	1.83 ± 0.02	2.24 ± 0.02	-

4. Conclusion and perspectives

A numerical simulation of soot particles aggregation and surface growth is performed by a Monte Carlo Discrete Element Method in a laminar premixed flame. The role played by soot maturity evolution during time is explored by modeling the collision and sticking probabilities as well as the evolution of the primary particle bulk density. The possible impact of the electrostatic repulsion of soot particles has also been investigated. Numerical results showed that both the particle maturity and the electrostatic forces affect the value of the collision and sticking probabilities. One raised questions was the evaluation of a critical primary diameter from which the sticking probability achieves its asymptotic value (unity). We evaluated this critical diameter around $d_s = 10$ nm for mature and nascent soot. However, when coupling these probabilities within the Monte Carlo Aggregation Code, it appears that inter-particle interactions do not considerably influence soot aggregation kinetics, particle size distribution, and morphology. This because the sticking probability of soot particles tends toward 1 in a very short period of time (a few miliseconds) that corresponds to a low collision frequency due to the very low soot volume fraction ($\sim 10^{-3}$ ppm) at this time. Therefore, under the studied conditions, we conclude that the assumption of a sticking probability = 1 is valid all along the soot formation process for soot particles even if the simulation begins with particles as small as $d_p = 2.4$ nm, which is lower than d_s. This tends to neglect the role played by electrostatic forces at short ranges as well as the effect of maturation on the collision and sticking probabilites in the simulation of aggregates formation for example by solving the population balance equation as in Ref. [50]. This also explains why most classical DLCA codes, where a sticking probability = 1 is assumed, succeed to produce fractal-like aggregates quite in good agreement with those measured experimentally under different flames conditions and fuel types [51–54]. Also, classical RLCA simulations show that a relevant variation in aggregates morphology (at least in terms of the fractal dimension) is found for extremely low sticking probability in the order of 10^{-3} [55–57] which is far to be representative of soot formation even when soot particles are still nascent.

However, the variation of soot particles bulk density due to maturity evolution in time has been shown to significantly influence the kinetics of agglomeration and thus the related coagulation kernels. Therfore we recommand to consider the variation of the bulk density from nascent to mature soot in numerical simulations of nanoparticles formation in flames. This is explained by an increased mobility of the particles having a lower bulk density. Nevertheless, this seems not to have a significant impact on the resulting particles morphology.

Finally, the updated version of MCAC is available under the following website https://gitlab.coria-cfd.fr/MCAC/MCAC/-/releases.

Acknowledgments

The authors gratefully acknowledge the support provided by ANR ASTORIA under the research grant ANR-18-CE05-0015 and the Region of Normandy RIN Gaspropres project. The authors also thank the CRIANN numerical resources supported by the Normandy region. C. Henry acknowledge the OPAL infrastructure from Université Côte d'Azur and Inria Sophia Antipolis - Méditerranée "NEF" computation platform for providing resources and support.

References

[1] H. Wang, Formation of nascent soot and other condensed-phase materials in flames, Proc. Combust. Inst. 33 (2011) 41–67.

[2] C. A. Schuetz, M. Frenklach, Nucleation of soot: molecular dynamics simulations of pyrene dimerization, Proc. Combust. Inst. 29 (2002) 2307–2314.

[3] A. Violi, S. Izvekov, Soot primary particle formation from multiscale coarse-grained molecular dynamics simulation, Proc. Combust. Inst. 31 (2007) 529–537.

[4] S. L. Fiedler, S. Izvekov, A. Violi, The effect of temperature on nanoparticle clustering, Carbon 45 (2007) 1786–1794.

[5] A. D'Anna, M. Sirignano, J. Kent, A model of particle nucleation in premixed ethylene flames, Combust. Flame 157 (2010) 2106–2115.

[6] Q. Mao, A. C. Van Duin, K. Luo, Formation of incipient soot particles from polycyclic aromatic hydrocarbons: a reaxff molecular dynamics study, Carbon 121 (2017) 380–388.

[7] A. Violi, A. F. Sarofim, G. A. Voth, Kinetic monte carlo–molecular dynamics approach to model soot inception, Combustion science and technology 176 (2004) 991–1005.

[8] D. Chen, K. H. Luo, Reactive sites on the surface of polycyclic aromatic hydrocarbon clusters: A numerical study, Combustion and Flame 211 (2020) 362–373.

[9] K. Bowal, L. Pascazio, H. Wang, D. Chen, M. Kraft, Surface properties of heterogeneous polycyclic aromatic hydrocarbon clusters, Proceedings of the Combustion Institute 38 (2021) 1115–1123.

[10] D. Chen, T. S. Totton, J. W. Akroyd, S. Mosbach, M. Kraft, Size-dependent melting of polycyclic aromatic hydrocarbon nano-clusters: A molecular dynamics study, Carbon 67 (2014) 79–91.

[11] L. Pascazio, J. W. Martin, K. Bowal, J. Akroyd, M. Kraft, Exploring the internal structure of soot particles using nanoindentation: A reactive molecular dynamics study, Combustion and Flame 219 (2020) 45–56.

[12] A. Sharma, K. M. Mukut, S. P. Roy, E. Goudeli, The coalescence of incipient soot clusters, Carbon 180 (2021) 215–225.

[13] T. S. Totton, A. J. Misquitta, M. Kraft, A quantitative study of the clustering of polycyclic aromatic hydrocarbons at high temperatures, Physical chemistry chemical physics 14 (2012) 4081–4094.

[14] S. Tang, J. Preece, C. McFarlane, Z. Zhang, Fractal morphology and breakage of dlca and rlca aggregates, J. Colloid Interface Sci. 221 (2000) 114–123.

[15] D. Hou, D. Zong, C. S. Lindberg, M. Kraft, X. You, On the coagulation efficiency of carbonaceous nanoparticles, J. Aerosol Sci. 140 (2020) 105478.

[16] H. A. Michelsen, Effects of maturity and temperature on soot density and specific heat, Proc. Combust. Inst. (2020).

[17] F.-X. Ouf, S. Bourrous, S. Fauvel, A. Kort, L. Lintis, J. Nuvoli, et al., True density of combustion emitted particles: A comparison of results highlighting the influence of the organic contents, J. Aerosol Sci. 134 (2019) 1–13.

[18] C. Russo, A. Tregrossi, A. Ciajolo, Dehydrogenation and growth of soot in premixed flames, Proc. Combust. Inst. 35 (2015) 1803–1809.

[19] A. Baldelli, U. Trivanovic, T. A. Sipkens, S. N. Rogak, On determining soot maturity: A review of the role of microscopy-and spectroscopy-based techniques, Chemosphere 252 (2020) 126532.

[20] J. Yon, J. J. Cruz, F. Escudero, J. Morán, F. Liu, A. Fuentes, Revealing soot maturity based on multi-wavelength absorption/emission measurements in laminar axisymmetric coflow ethylene diffusion flames, Combust. Flame 227 (2021) 147–161.

[21] A. D'Alessio, A. Barone, R. Cau, A. D'Anna, P. Minutolo, Surface deposition and coagulation efficiency of combustion generated nanoparticles in the size range from 1 to 10 nm, Proc. Combust. Inst. 30 (2005) 2595–2603.

[22] A. B. Fialkov, Investigations on ions in flames, Prog. Energy Combust. Sci. 23 (1997) 399–528.

[23] M. Maricq, Size and charge of soot particles in rich premixed ethylene flames, Combust. Flame 137 (2004) 340–350.

[24] A. Starik, A. Savel'ev, N. Titova, Formation of charged nanoparticles in

hydrocarbon flames: principal mechanisms, Plasma Sources Sci. Technol. 17 (2008) 045012.

[25] M. M. Maricq, Thermal equilibration of soot charge distributions by coagulation, J. Aerosol Sci. 39 (2008) 141–149.

[26] H. Mätzing, W. Baumann, H. Bockhorn, H.-R. Paur, H. Seifert, Detection of electrically charged soot particles in laminar premixed flames, Combust. Flame 159 (2012) 1082–1089.

[27] C. Henry, J.-P. Minier, J. Pozorski, G. Lefèvre, A new stochastic approach for the simulation of agglomeration between colloidal particles, Langmuir 29 (2013) 13694–13707.

[28] J. Morán, J. Yon, A. Poux, Monte carlo aggregation code (mcac) part 1: Fundamentals, J. Colloid Interface Sci. 569 (2020) 184–194.

[29] J. Morán, J. Yon, A. Poux, F. Corbin, F.-X. Ouf, A. Siméon, Monte carlo aggregation code (mcac) part 2: Application to soot agglomeration, highlighting the importance of primary particles, J. Colloid Interface Sci. 575 (2020) 274–285.

[30] J. Morán, A. Poux, J. Yon, Impact of the competition between aggregation and surface growth on the morphology of soot particles formed in an ethylene laminar premixed flame, J. Aerosol Sci. 152 (2021) 105690.

[31] A. M. Starik, A. M. Savel'ev, N. S. Titova, U. Schumann, Modeling of sulfur gases and chemiions in aircraft engines, Aerospace Science and Technology 6 (2002) 63–81.

[32] A. Onischuk, S. Di Stasio, V. Karasev, A. Baklanov, G. Makhov, A. Vlasenko, A. Sadykova, A. Shipovalov, V. Panfilov, Evolution of structure and charge of soot aggregates during and after formation in a propane/air diffusion flame, Journal of aerosol science 34 (2003) 383–403.

[33] M. Balthasar, F. Mauß, H. Wang, A computational study of the thermal ionization of soot particles and its effect on their growth in laminar premixed flames, Combustion and flame 129 (2002) 204–216.

[34] M. M. Maricq, The dynamics of electrically charged soot particles in a premixed ethylene flame, Combustion and flame 141 (2005) 406–416.

[35] M. M. Maricq, A comparison of soot size and charge distributions from ethane, ethylene, acetylene, and benzene/ethylene premixed flames, Combustion and flame 144 (2006) 730–743.

[36] J. Prager, U. Riedel, J. Warnatz, Modeling ion chemistry and charged species diffusion in lean methane–oxygen flames, Proceedings of the Combustion Institute 31 (2007) 1129–1137.

[37] F. Babick, K. Schießl, M. Stintz, van-der-waals interaction between two fractal aggregates, Adv. Powder Technol. 22 (2011) 220–225.

[38] C. Henry, J.-P. Minier, G. Lefèvre, Towards a description of particulate fouling: From single particle deposition to clogging, Adv. Colloid Interface Sci. 185 (2012) 34–76.

[39] P. Meakin, Reaction-limited cluster-cluster aggregation in dimensionalities 2–10, Phys. Rev. A 38 (1988) 4799.

[40] S. Lazzari, M. Lattuada, Growth and aggregation regulate clusters structural properties and gel time, J. Phys. Chem. B 121 (2017) 2511–2524.

[41] J. Morán, J. Cuevas, F. Liu, J. Yon, A. Fuentes, Influence of primary particle polydispersity and overlapping on soot morphological parameters derived from numerical tem images, Powder Technol. 330 (2018) 67–79.

[42] F. Cazals, H. Kanhere, S. Loriot, Computing the volume of a union of balls: a certified algorithm, ACM Trans. Math. Softw. 38 (2011) 1–20. doi:`https://doi.org/10.1145/2049662.2049665`.

[43] J. Morán, A. Fuentes, F. Liu, J. Yon, Fracval: An improved tunable algorithm of cluster–cluster aggregation for generation of fractal structures formed by polydisperse primary particles, Comput. Phys. Commun. 239 (2019) 225–237.

[44] J. Yon, J. Morán, F.-X. Ouf, M. Mazur, J. Mitchell, From monomers to agglomerates: A generalized model for characterizing the morphology of fractal-like clusters, J. Aerosol Sci. 151 (2021) 105628.

[45] A. Abid, E. Tolmachoff, D. Phares, H. Wang, Y. Liu, A. Laskin, Size distribution and morphology of nascent soot in premixed ethylene flames with and without benzene doping, Proc. Combust. Inst. 32 (2009) 681–688.

[46] S. De Iuliis, S. Maffi, F. Migliorini, F. Cignoli, G. Zizak, Effect of hydrogen addition on soot formation in an ethylene/air premixed flame, Appl. Phys. B 106 (2012) 707–715.

[47] F. Pierce, C. Sorensen, A. Chakrabarti, Computer simulation of diffusion-limited cluster-cluster aggregation with an epstein drag force, Phys. Rev. E 74 (2006) 021411.

[48] S. De Iuliis, S. Maffi, F. Cignoli, G. Zizak, Three-angle scattering/extinction versus tem measurements on soot in premixed ethylene/air flame, Appl. Phys. B 102 (2011) 891–903.

[49] M. Altenhoff, S. Aßmann, C. Teige, F. J. Huber, S. Will, An optimized evaluation strategy for a comprehensive morphological soot nanoparticle aggregate characterization by electron microscopy, J. Aerosol Sci. 139 (2020) 105470.

[50] N. A. Eaves, Q. Zhang, F. Liu, H. Guo, S. B. Dworkin, M. J. Thomson, Coflame: A refined and validated numerical algorithm for modeling sooting laminar coflow diffusion flames, Comput. Phys. Commun. 207 (2016) 464–477.

[51] C. M. Megaridis, R. A. Dobbins, Morphological description of flame-generated materials, Combust. Sci. Technol. 71 (1990) 95–109.

[52] C. Sorensen, G. Feke, The morphology of macroscopic soot, Aerosol Sci. Technol. 25 (1996) 328–337.

[53] M. Lapuerta, F. J. Martos, G. Martín-González, Geometrical determination of the lacunarity of agglomerates with integer fractal dimension, J. Colloid Interface Sci. 346 (2010) 23–31.

[54] D. Cortés, J. Morán, F. Liu, F. Escudero, J.-L. Consalvi, A. Fuentes,

Effect of fuels and oxygen indices on the morphology of soot generated in laminar coflow diffusion flames, Energy Fuels 32 (2018) 11802–11813.

[55] D. Weitz, J. Huang, M. Lin, J. Sung, Limits of the fractal dimension for irreversible kinetic aggregation of gold colloids, Phys. Rev. Lett. 54 (1985) 1416.

[56] P. Meakin, F. Family, Structure and kinetics of reaction-limited aggregation, Phys. Rev. A 38 (1988) 2110.

[57] M. Lattuada, H. Wu, M. Morbidelli, A simple model for the structure of fractal aggregates, J. Colloid Interface Sci. 268 (2003) 106–120.

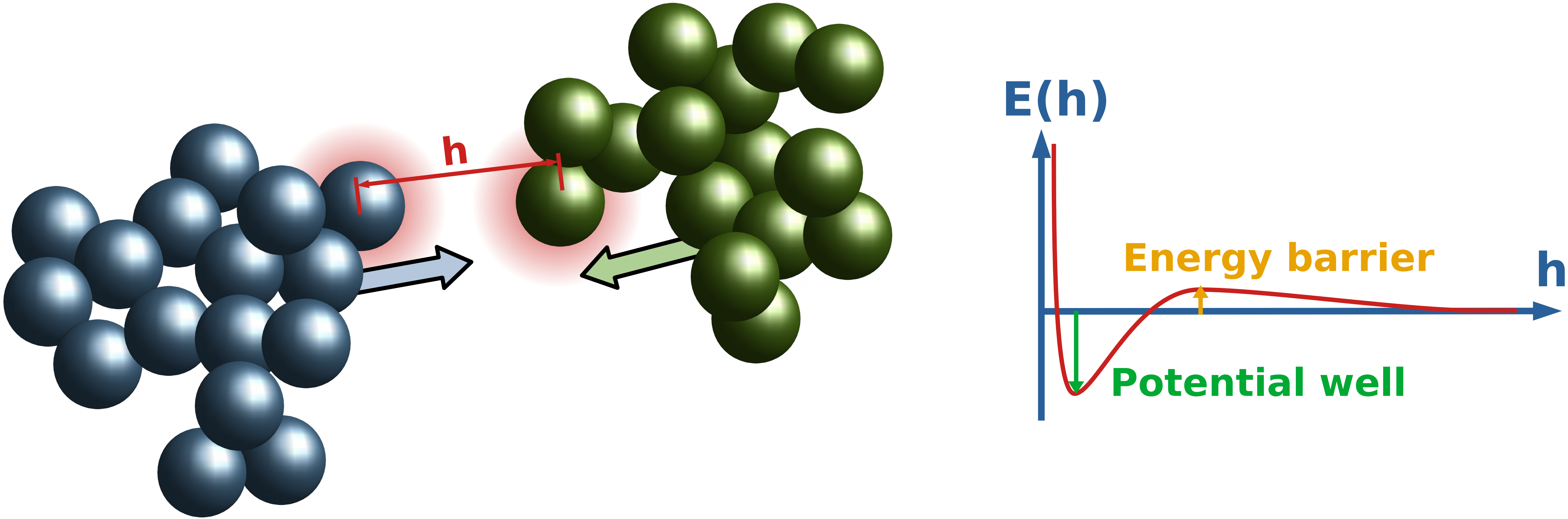
h
E(h)
Energy barrier
h
Potential well